ACADEMIC PRESS

Available online at www.sciencedirect.com

SCIENCE DIRECT®

Journal of Computational Physics 186 (2003) 230–249

JOURNAL OF COMPUTATIONAL PHYSICS

www.elsevier.com/locate/jcp

Computing unstable manifolds of periodic orbits in delay differential equations

Bernd Krauskopf *, Kirk Green

Department of Engineering Mathematics, University of Bristol, Queen's Building, Bristol BS8 1TR, UK

Received 24 January 2001; received in revised form 26 June 2002; accepted 10 January 2003

Abstract

We present the first algorithm for computing unstable manifolds of saddle-type periodic orbits with one unstable Floquet multiplier in systems of autonomous delay differential equations (DDEs) with one fixed delay. Specifically, we grow the one-dimensional unstable manifold $W^{u}(q)$ of an associated saddle fixed point q of a Poincaré map defined by a suitable Poincaré section Σ. Starting close to q along the linear approximation to $W^{u}(q)$ given by the associated eigenfunction, our algorithm grows the manifold as a sequence of points, where the distance between points is governed by the curvature of the one-dimensional intersection curve $W^{u}(q) \cap \Sigma$ of $W^{u}(q)$ with Σ. Our algorithm makes it possible to study global bifurcations in DDEs. We illustrate this with the break-up of an invariant torus and a subsequent crisis bifurcation to chaos in a DDE model of a semiconductor laser with phase-conjugate feedback.

Keywords: Delay differential equations; Unstable manifold computation; Lasers with feedback

1. Introduction

Delay differential equations (DDEs) have received a lot of attention recently, because models featuring a delay term appear in areas of application as diverse as biology [28], neural networks [27] and control theory [12]. Of particular technological importance are DDEs describing semiconductor lasers subject to delayed feedback [20]. Semiconductor lasers are widely used today, and delay arises naturally, for example, due to reflections on a CD or optical fiber. Apart from this case of so-called conventional optical feedback (COF) [10,11,26], other examples of lasers with delay are mutually coupled lasers [17], lasers with opto-electronic feedback [35], and lasers with phase-conjugate feedback (PCF) [1,13,19,25]. The latter system will serve as the illustrating example, and it is introduced in Section 4.

The fundamental difficulty is that the phase space of a DDE is infinite-dimensional. We restrict ourselves here to the important special case of an autonomous DDE with a single fixed delay; for example, all laser systems just mentioned are of this form. For this class of DDEs the local bifurcation theory is quite well

* Corresponding author.
E-mail addresses: B.Krauskopf@bristol.ac.uk (B. Krauskopf), Kirk.Green@bristol.ac.uk (K. Green).

0021-9991/03/$ - see front matter
doi:10.1016/S0021-9991(03)00050-0

established; the relevant concepts are introduced in Section 2. However, it is difficult to apply this theory to DDE models arising in applications, and the most one can hope for is a stability analysis of equilibria. Until very recently, the only other way to study DDEs was by simulation, that is, by numerical integration; see also Section 2.1.

The good news is, that this is now changing dramatically with the arrival of continuation software, notably the package DDE-BIFTOOL [7–9], which allows the user to find and follow equilibria and periodic orbits irrespective of their stability. Changes of the stability (local codimension-one bifurcations) can be detected and also followed as parameters are varied; see Section 2.5. DDE-BIFTOOL essentially implements the local bifurcation theory of DDEs and has roughly the same functionality that the local bifurcation theory part of the well-known continuation package AUTO [5] has for ordinary differential equations (ODEs). DDE-BIFTOOL is still under development with new capabilities being added; one is the continuation of homoclinic and heteroclinic orbits to equilibria [32].

As is known from the respective theory for ODEs, the next step is to understand the global dynamics of a DDE. To this end one needs to find not only saddle points and saddle periodic orbits, but also their global stable and unstable manifolds. Except in the case of a one-dimensional unstable manifold of an equilibrium [14] (see Section 2.2), they cannot be found by mere integration, but require more sophisticated methods.

In this paper, we make a step in this direction and present the first method to compute global unstable manifolds of saddle periodic orbits with one unstable Floquet multiplier in autonomous DDEs with one fixed delay. Specifically, we compute the one-dimensional unstable manifold of a saddle fixed point in a suitable Poincaré map, which corresponds to a saddle periodic orbit of the DDE; see Section 3 for details. We remark that we speak of a one-dimensional unstable manifold to stress that there is only one unstable eigenfunction. The unstable manifold of a periodic orbit of a DDE is a two-dimensional object in an infinite-dimensional space, but one whose intersection with the Poincaré plane is a one-dimensional curve.

The basic idea is to generalize the method for finite-dimensional maps in [23] (now implemented in the DSTOOL environment [2]) to the setting of DDEs. We use DDE-BIFTOOL to obtain the starting data required by our method. At present, the implementation is stand-alone, but it is envisaged that it will be integrated with DDE-BIFTOOL. Our method computes a piece of the unstable manifold of a set arclength, represented by a minimum number of points while satisfying pre-specified accuracy parameters. While the unstable manifold is a complicated object, its intersection with the Poincaré section, which we call the trace, is a one-dimensional curve. Despite effects of projection from an infinite-dimensional space, this curve conveys basically the same information as a one-dimensional unstable manifold of a fixed point of a planar map. This allows one to identify and study, for the first time, global bifurcations in DDEs. As an example, we show in Section 4 the break-up of a torus in the PCF laser and its subsequent transition to chaos in a crisis bifurcation.

2. Background on DDEs

We now recall some basic facts on DDEs; see [4,16,34] as general references to the theory. Readers may find it useful to look ahead to the concrete example of a laser with phase-conjugate feedback, system (10) in Section 4, which is used for illustration throughout. We consider the simplest case, namely an autonomous DDE with a single fixed delay. It has the general form

$$\frac{\mathrm{d}x(t)}{\mathrm{d}t} = F(x(t), x(t-\tau), \lambda), \tag{1}$$

where

$$F : \mathbb{R}^n \times \mathbb{R}^n \times \mathbb{R}^p \to \mathbb{R}^n$$

is differentiable and where $\tau \in \mathbb{R}$ is a fixed delay, while $\lambda \in \mathbb{R}^p$ represents a number of physical parameters. Considering a single fixed delay is less of a restriction than it seems: for example, all of the laser systems mentioned in Section 1 are in this class. Furthermore, the algorithm described in Section 3 also works for delay equations with a finite number of fixed delays, by way of working with the largest such delay. Other types of delay, such as state dependent delays, are beyond the scope of this paper.

Like it is the case for finite-dimensional vector fields, the function F assigns at a given moment t in time a vector, but this vector now not only depends on the state $x(t)$ but also on $x(t-\tau)$ at time τ earlier. The solution of (1) is a function

$$x : [-\tau, \infty) \to \mathbb{R}^n, \tag{2}$$

which is a one-parameter family of vectors $x(t)$ defined only for all positive values of time t. We call $\mathbb{R}^n$ the *physical space* of the system, but the crucial thing is that $\mathbb{R}^n$ is *not* the phase space of (1). Indeed, one needs to know the entire *history* of $x(0)$, that is, a continuous function on the interval $[-\tau, 0]$ for (1) to have a unique solution. In other words, the phase space of (1) is the infinite-dimensional space of continuous functions with values in the physical space $\mathbb{R}^n$, denoted by $\mathscr{C}$. When we speak of a *point*, say $q \in \mathscr{C}$, in what follows we mean a point in this infinite-dimensional phase space, that is, q is a continuous function

$$q : [-\tau, 0] \to \mathbb{R}^n.$$

Further, we call $q(0)$ the head of q and $\{q(t) \,|\, t \in [-\tau, 0)\}$ its history.

The *evolution operator*

$$\Phi^t : \mathscr{C} \to \mathscr{C} \tag{3}$$

describes how an initial condition $q \in \mathscr{C}$ evolves after time t. It is formally given by an abstract differential equation on the infinite-dimensional phase space [6]. More geometrically, one can picture Φ^t as illustrated in Fig. 1. The point q is mapped under Φ^t to a new point $\Phi^t(q)$. If one imagines letting time t run then $\Phi^t(q)$ moves over the solution x of (1) like a train over a roller coaster track.

In general, the flow is not defined for negative time. However, for special solutions, such as periodic orbits and their stable and unstable manifolds, the flow can be defined also for negative time; see e.g. [16].

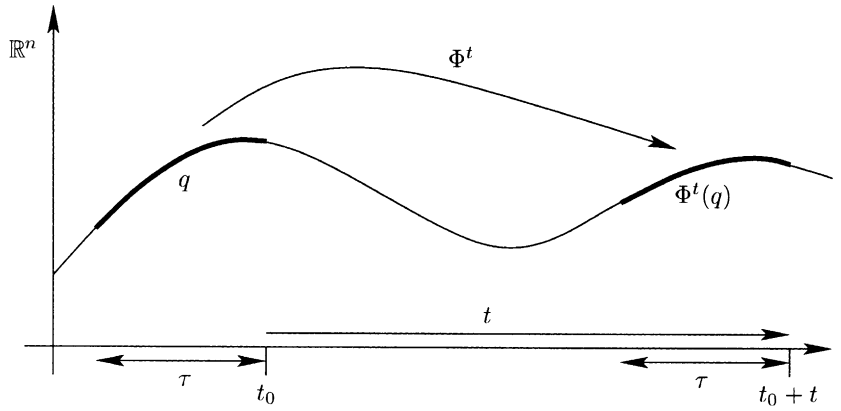

Fig. 1. The evolution operator Φ^t of a DDE takes a point q to $\Phi^t(q)$ for any positive $t > 0$. In projection onto the physical space $\mathbb{R}^n$, the point q is a finite piece of curve that is transported under Φ^t much like a train moving over a roller coaster track.

2.1. Numerical integration

A DDE of the form (1) with a fixed delay can easily be integrated numerically with a fixed time-step method, where the time-step is such that it fits an integer number of times into the delay time τ. To this end, one discretizes the history of every point, that is, the interval $[-\tau, 0]$, into M subintervals. Here the integer M is chosen such that the integration step τ/M is sufficiently small. This induces a discretization of time t into steps of τ/M, yielding a numerical approximation of the evolution operator $\Phi^{\tau/M}$ as the basic integration step.

It is particularly useful to represent a point q by a circular list as is shown in Fig. 2(a), where **root** points to the headpoint $q(0)$ of q. In the simplest case of an Euler integration step, the point $q(-\tau)$ is simply overwritten by the new headpoint $q(\tau/M)$ of $\Phi^{\tau/M}(q)$ and **root** moves one node along the circular list. In our simulations we use an Adams–Bashforth fourth-order multistep method, which requires storing a list up to and including the vector $q(-\tau - 3(\tau/M))$.

2.2. Equilibria

The simplest invariant object of (1) is an *equilibrium* point $x(t) = x_0$ for all $t \in [0, \infty]$ and fixed $x_0 \in \mathbb{R}^n$, which satisfies $F(x_0, x_0, \lambda^*) = 0$ (where the parameter is now fixed to λ^*). Its stability is determined by the eigenvalues of the linearization $DF(x_0, x_0, \lambda^*) = Ax(t) + Bx(t-\tau)$ around x_0, where $A = D_1F(x_0, x_0, \lambda^*)$ and $B = D_2F(x_0, x_0, \lambda^*)$ are the derivatives of F in (1) with respect to the first and second variable. The spectrum of the operator DF consists only of eigenvalues and is given by the roots of the characteristic function $\chi(\lambda) = \det(\lambda I - A - Be^{-\lambda\tau})$. Furthermore, it is an important property that the eigenvalues are discrete and there are at most finitely many unstable eigenvalues; see e.g. [16,34] for more details. One says that an equilibrium x_0 is hyperbolic, if $DF(x_0, x_0, \lambda^*)$ has no eigenvalues with zero real part. A hyperbolic equilibrium x_0 is either stable, namely if all of these eigenvalues have real part less than zero, or a saddle otherwise. In the latter case one can consider the *local unstable manifold* $W^{\mathrm{u}}_{\mathrm{loc}}(x_0)$, which is the set of points q that can be integrated backwards, never leave a small neighborhood V of x_0 under Φ^t for $t < 0$ and are such that $\Phi^t(q) \to x_0$ as $t \to -\infty$. The local unstable manifold $W^{\mathrm{u}}_{\mathrm{loc}}(x_0)$ is finite-dimensional and tangent to the linear eigenspace $E^{\mathrm{u}}(x_0)$ spanned by the unstable eigenfunctions. The (global) unstable manifold $W^{\mathrm{u}}(x_0)$ is

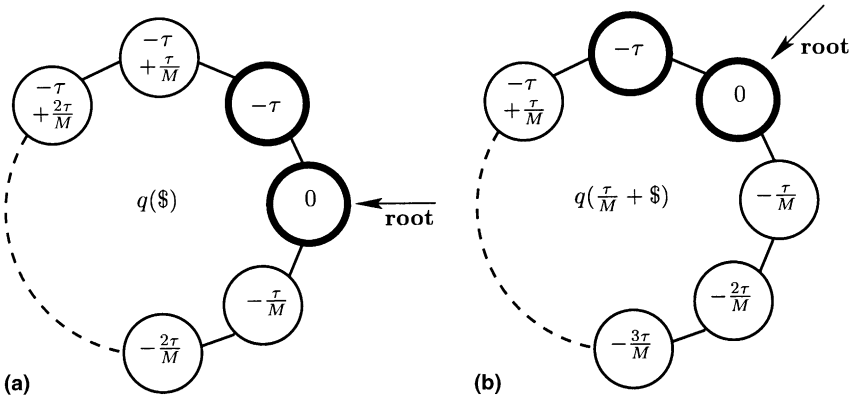

Fig. 2. One Euler integration step applied to the circular list representing a point of a DDE. The delay interval is discretized into $M + 1$ elements, with \$ standing for the labels of the list elements. Before the integration step **root** points to $q(0)$ (a), and after the integration step **root** points to $q(\tau/M)$, which can be achieved by simply overwriting $q(-\tau)$ and moving **root** (b). Only the two boldfaced list elements close to **root** are needed for one Euler step.

defined as $W^{\mathrm{u}}(x_0) = \{\Phi^t(p) \,|\, p \in W^{\mathrm{u}}_{\mathrm{loc}}(x_0) \text{ and } t > 0\}$. The stable manifold $W^{\mathrm{s}}(x_0)$ is defined similarly as the set of points that converge to x_0 under Φ^t in positive time. Note that $W^{\mathrm{s}}(x_0)$ is always infinite-dimensional.

When there is one unstable eigenvalue then the unstable manifold $W^{\mathrm{u}}(x_0)$ is a smooth one-dimensional curve in projection onto the physical space $\mathbb{R}^n$. Both of its branches can be found by integrating two initial conditions near x_0 along the linear eigenspace $E^{\mathrm{u}}(x_0)$. Approximations to both x_0 and $E^{\mathrm{u}}(x_0)$ can be found with the continuation software DDE-BIFTOOL; see Section 2.5. Examples of one-dimensional unstable manifolds of equilibria can be found in [14].

It is much harder to compute higher-dimensional unstable manifolds of equilibria. It appears to be possible that methods from ODEs [24] can be generalized to the DDEs case, but this is work for the future. The main interest here is in computing the one-dimensional unstable manifold of a saddle point of the Poincaré map associated with a given periodic orbit.

2.3. Periodic orbits and the Poincaré map of a DDE

A *periodic point* of (1) is a solution $q \in \mathscr{C}$ such that $\Phi^{\mathsf{T}}(q) = q$ for some (smallest) period $\mathsf{T} > 0$. The associated solution $\Gamma(t)$ starting from q is a *periodic orbit*. In other words, a periodic orbit is a solution along which any segment of length τ repeats after time T. The periodic orbit Γ traces out a closed curve in projection onto the physical space $\mathbb{R}^n$.

A very useful concept is that of the *Poincaré* map P defined by the return to a suitable section transverse to the flow of (1). For a prescribed section $\Sigma \subset \mathbb{R}^n$ we denote by $\mathscr{C}_\Sigma$ the space of points in $\mathscr{C}$ with headpoints in Σ. Then the Poincaré map P is defined as

$$P: \ \mathscr{C}_\Sigma \to \mathscr{C}_\Sigma, \quad q \mapsto \Phi^{t_q}(q), \tag{4}$$

where $t_q > 0$ is the return time to Σ. In other words, the headpoint of $P(q)$ again lies in the section Σ, as is illustrated in Fig. 3.

One can always find a section Σ (locally) transverse to a periodic orbit Γ, so that the Poincaré map is well defined at least locally near the intersection point with Σ, which is a fixed point $q \in \mathscr{C}_\Sigma$ under P (and a periodic point of (1) as defined above); see Fig. 4.

The stability of a periodic orbit Γ is given by its Floquet multipliers, which are the eigenvalues of the linearization $DP(q)$ of the Poincaré map P at the associated fixed point $q \in \mathscr{C}_\Sigma$. The linearization $DP(q)$ is a

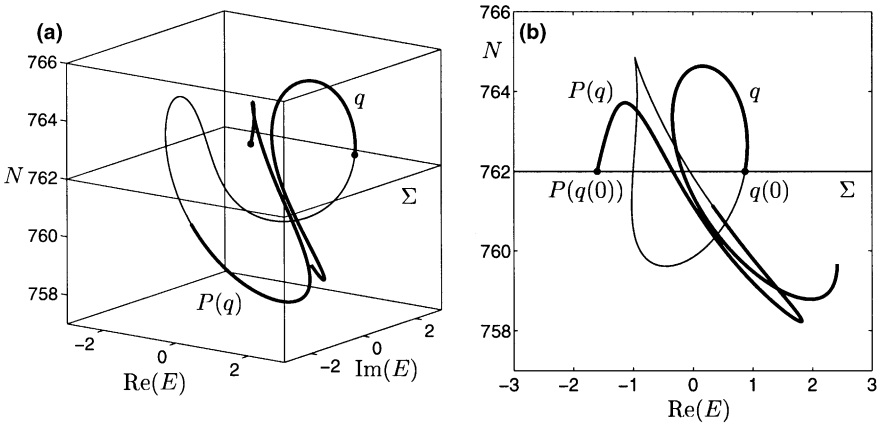

Fig. 3. The Poincaré map P takes a point q with $q(0) \in \Sigma$ to the point $P(q)$ with $P(q(0)) \in \Sigma$, which is shown in (E, N)-space (a) and in the $(\mathrm{Re}(E), N)$-plane (b) for the PCF laser (10).

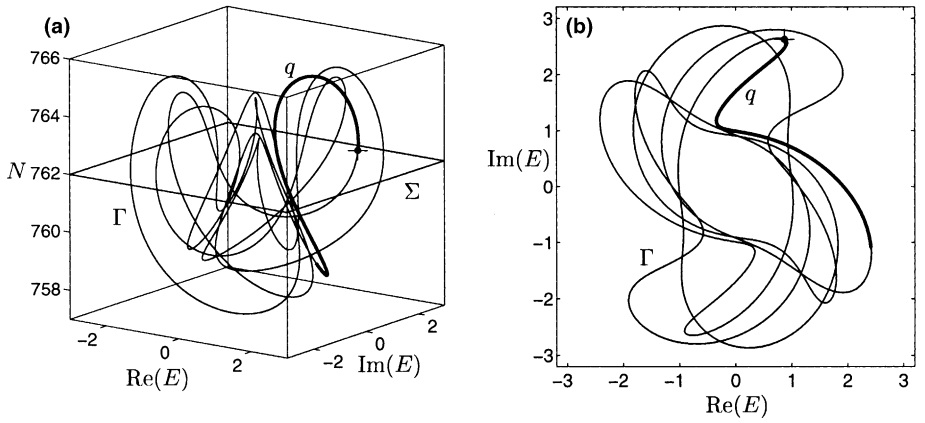

Fig. 4. A periodic orbit Γ of the DDE and a periodic point q of the Poincaré map P (boldface), shown in (E,N)-space (a) and in the E-plane (b) for the PCF laser (10).

compact operator, which implies that its spectrum consists of countably many eigenvalues (the Floquet multipliers) with the origin of the complex plane as their only possible accumulation point; see e.g. [16,34] for more details. It follows that for any fixed $r > 0$ there is only a finite number of Floquet multipliers outside a circle of radius r. In particular, there are always only a finite number of unstable Floquet multipliers, that is Floquet multipliers outside the unit circle. A periodic orbit is called hyperbolic if there are no Floquet multipliers on the unit circle. A hyperbolic periodic orbit is either stable if all the Floquet multipliers are inside the unit circle or of saddle type with finitely many unstable Floquet multipliers.

If there are other Floquet multipliers on the unit circle then the system is undergoing a bifurcation. In Section 4 we will encounter saddle-node, symmetry-breaking and torus (or Neimark–Sacker) bifurcations, which are all associated with Floquet multipliers crossing the unit circle.

We now briefly discuss how one can compute the Poincaré map P in practice. Near q the map P can be defined as the kth return to the section Σ for some fixed k, where k counts all intersections of the periodic orbit with Σ (of which $k-1$ are outside a small neighborhood of q). It is generally not possible to define P *globally* as the kth return map to Σ for a fixed k. Indeed there typically are curves in Σ along which the flow fails to be transverse, and this changes the number of returns to Σ. (This is in contrast to periodically forced systems, which do have a globally defined Poincaré map in the form of the stroboscopic map of the forcing frequency.) Such a tangency can occur at the begin point, an interior point or the end point of the orbit of the flow. In our computations we deal with the case that a tangency occurs at an interior point: we detect it and change the definition of P from being the kth to the $(k+2)$th (or the $(k-2)$th) return to Σ. This is done by monitoring the return time to Σ, which is a continuous function across this tangency. Indeed discontinuities of the kth return map are encountered when computing a global object such as an unstable manifold, and dealing with them as just explained allows us to compute longer pieces of manifolds; see Section 4.3 for an example.

2.4. Unstable manifold of a fixed point

Suppose that a periodic orbit has Floquet multipliers outside the unit circle. For a suitable section Σ transverse to the periodic orbit we consider the fixed point $q \in \mathscr{C}_\Sigma$ (with headpoint in Σ) of the associated Poincaré map P. The *local unstable manifold* $W^{\mathrm{u}}_{\mathrm{loc}}(q)$ of q is the set of all points $p \in \mathscr{C}_\Sigma$ that can be iterated backwards under P, never leave a small neighborhood V of q and are such that $P^l(p) \to q$ as $l \to -\infty$. The local unstable manifold $W^{\mathrm{u}}_{\mathrm{loc}}(q)$ is finite-dimensional and tangent to the linear eigenspace $E^{\mathrm{u}}(q)$ spanned by

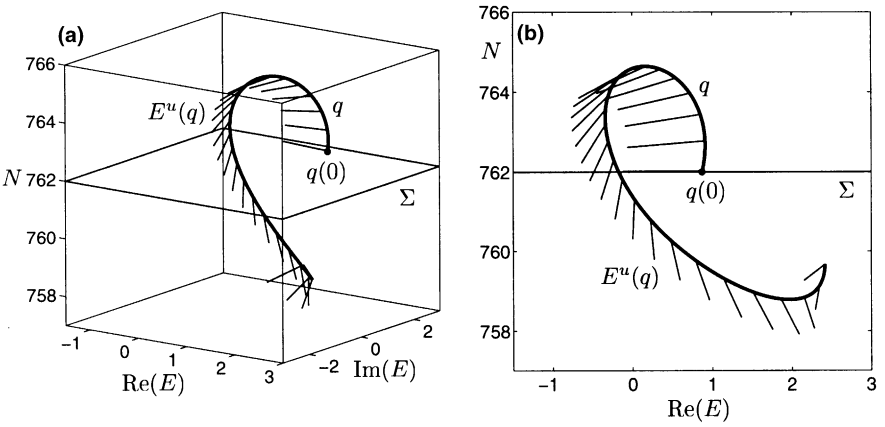

Fig. 5. A periodic point of saddle-type q together with the linear line field approximating the unstable linear eigenspace (only every 100th line of the discrete representation is shown), shown in (E,N)-space (a) and in the $(\mathrm{Re}(E),N)$-plane (b) for the PCF laser (10).

the unstable eigenfunction. In the case that there is a single Floquet multiplier outside the unit circle then, in projection onto the physical space $\mathbb{R}^n$, the one-dimensional linear eigenspace $E^{\mathrm{u}}(q)$ forms a one-parameter family of directions along (the history of) q, as is illustrated in Fig. 5. The (global) unstable manifold $W^{\mathrm{u}}(q)$ can be defined as $W^{\mathrm{u}}(q) = \{P^l(p) \,|\, p \in W^{\mathrm{u}}_{\mathrm{loc}}(q) \text{ and } l > 0\}$.

The stable manifold $W^{\mathrm{s}}(q)$ is defined similarly as the set of points that converge to q under P in positive time. Again, $W^{\mathrm{s}}(q)$ is always infinite-dimensional.

In projection onto the physical space $\mathbb{R}^n$ a one-dimensional unstable manifold $W^{\mathrm{u}}(q)$ forms a complicated object; see already Fig. 11 below. However, its *trace* $W^{\mathrm{u}}(q) \cap \Sigma$ is a one-dimensional curve that is smooth (except possibly at isolated points due to the projection). The trace of the one-dimensional unstable manifold $W^{\mathrm{u}}(q)$ reveals about as much as a one-dimensional unstable manifold of a diffeomorphism in $\mathbb{R}^2$; see Section 4.3. We remark that the trace may have self-intersections. This is an artifact of the projection and reminds one of the fact that $W^{\mathrm{u}}(q)$ lives in an infinite-dimensional phase space.

2.5. Numerical continuation

The recently developed continuation package DDE-BIFTOOL [7–9] goes far beyond simulation. DDE-BIFTOOL consists of Matlab routines for the continuation and bifurcation analysis of steady states and periodic solutions. Roughly speaking it has the same functionality for DDEs as (the local bifurcation part of) the well-known package AUTO [5] does for ODEs. It not only allows one to find and follow stable solutions (those also found by simulation), but unstable ones as well. Furthermore, DDE-BIFTOOL detects the codimension-one local bifurcations listed, namely saddle-node, Hopf, period-doubling, saddle-node of limit cycles, and torus bifurcations.

More specifically, DDE-BIFTOOL solves a large system that is obtained by discretizing the delay interval $[-\tau, 0]$ as described in Section 2.1. It uses arclength continuation to follow equilibria and periodic orbits as a parameter is varied. Periodic orbits are represented by a suitable boundary value problem, which is solved using Gauss collocation. By also solving for the eigenvalues, the above local bifurcations, for equilibria, are detected and can then be followed in two parameters; for further details see [7–9].

The usefulness of DDE-BIFTOOL can hardly be exaggerated. It enables continuation studies of local bifurcations in DDEs in much the same way as one is used to perform for ODEs. DDE-BIFTOOL has not been used that widely yet, but there are already some examples of its use in applications, for example, the study of a laser with COF in [30,31] and our own work on the PCF laser; see Section 4 and [14,15].

In the context of computing one-dimensional unstable manifolds of periodic orbits, DDE-BIFTOOL is crucial for finding periodic orbits with one unstable Floquet multiplier as starting data.

3. Computing one-dimensional unstable manifolds

Let $q \in \mathscr{C}_\Sigma$ be a saddle fixed point of a Poincaré map P defined by a section Σ transverse to the periodic orbit that corresponds to q. We further assume that the periodic orbit has exactly one unstable Floquet multiplier, so that the linearization $DP(q)$ of P has one unstable eigenvalue (which lies outside the unit circle). The goal is to compute the one-dimensional unstable manifold $W^{\mathrm{u}}(q)$.

The basic idea is to realize that practically any of the known algorithms for computing one-dimensional unstable manifolds of saddle points of finite-dimensional maps can be generalized to the setting of DDEs by working on points in $\mathscr{C}_\Sigma$, instead of on points in a finite-dimensional space. While this sounds simple, all relevant operations, such as the iteration of the Poincaré map and interpolation, need to be interpreted and implemented as operations on points in $\mathscr{C}_\Sigma$, or rather on their discretizations as circular lists. This can be done by applying all respective operations *pointwise* to the elements of the respective circular lists; see Fig. 2.

We chose to implement the generalization of the growth method in [23], because it computes the minimum number of points necessary to achieve an accurate representation of $W^{\mathrm{u}}(q)$ (according to prespecified accuracy parameters) by taking account of the curvature along the manifold. Using as few points as possible while maintaining a prescribed quality of the computation is particularly important in the setting of DDEs because every point in $\mathscr{C}$ is discretized and represented by a circular list of $(M+4)\times n$ real numbers; see Section 2.1. We remark that we do not adapt the integration step size during a computation, but use a fixed time step τ/M throughout.

3.1. Starting data

The starting data for a computation of an unstable manifold are the saddle periodic point q together with the knowledge of the linear eigenfunction $E^{\mathrm{u}}(q)$, which we represent by a (generalized) vector $v = \{v(t) \,|\, t \in [-\tau, 0]\}$ whose elements are unit vectors. Both of these objects are represented as circular lists of length $M+4$, because of the integration method we use; see Section 2.1.

The saddle periodic point q can be found as follows. With the help of DDE-BIFTOOL, one continues periodic orbits of the DDE until a suitable saddle periodic orbit with one unstable eigenvalue is found. From this orbit one extracts the saddle periodic point q by choosing a point $q(0)$ in the prescribed section Σ together with its history. Because the required headpoint $q(0)$ will generally not be part of the mesh used by DDE-BIFTOOL to represent the saddle periodic orbit, this step requires interpolation. Fig. 4 shows a periodic orbit Γ of saddle-type computed by continuation with DDE-BIFTOOL, on which a periodic point $q \in \mathscr{C}_\Sigma$ has been selected. Notice that Γ intersects the chosen section Σ twenty times, so that P can be defined locally near q as the 20th return to Σ.

The next step is to find the vector v, which is a circular list defining a direction at every discretization point of the delay interval. As finding v is not yet implemented in DDE-BIFTOOL, we use the following method. Choose a starting point close to q along some chosen direction v_0 and perform a small number m of iterations under the Poincaré map P, yielding $\widetilde{v}_1 = P^m(q+\eta v_0) - q$. Normalizing $\widetilde{v}_1$ such that each element of the circular list is a unit vector gives a first approximation v_1 of v. This process can be repeated, yielding the approximation $v_2 = (P^l(q+\eta v_1) - q)/|P^l(q+\eta v_1) - q|$, and so on until one is satisfied with the accuracy. In Fig. 5 we illustrate v by plotting its every 100th element.

We finally remark that the above procedure finds the unstable eigenfunction v of the *strongest* unstable eigenvalue when there are other unstable eigenvalues. In this case, the algorithm described below computes the strong unstable manifold, which is tangent to this vector v.

3.2. Growing the manifold

With the knowledge of (approximations to) q and v one can implement one's favorite method for computing the associated one-dimensional unstable manifold $W^{\mathrm{u}}(q)$; for example those in [18,22,23, 29,36].

The easiest method is *fundamental domain iteration*. Take a fixed number of points on the segment $P(q+\delta v)-(q+\delta v)$ and iterate them under the Poincaré map P. Because of its invariance, all iterates will lie on $W^{\mathrm{u}}(q)$ in good approximation. However, the distribution of points along $W^{\mathrm{u}}(q)$ is generally poor. Nevertheless, the computational error of these points is determined only by the initial distance δ along v and the accuracy of the integration, a fact that will be utilized in Section 4. There are several methods to ensure a suitable distribution of computed points along $W^{\mathrm{u}}(q)$ [18,29,36]; see also the discussion in [23].

The method we decided to generalize to the setting of DDEs is that in [23], which entirely steps away from the idea of using a fundamental domain. The manifold $W^{\mathrm{u}}(q)$ is represented by a list of points in $\mathscr{C}_\Sigma$ with the understanding that linear interpolation is used between consecutive points of this list. The idea is to find the next point p_{k+1} along $W^{\mathrm{u}}(q)$ at some distance Δ_k from the last point p_k. This is done by finding a pre-image $\hat{p}$ of p_{k+1} in the part of $W^{\mathrm{u}}(q)$ that was already computed. This idea is sketched in Fig. 6. The algorithm first finds the two points p_l and p_{l+1} between which $\hat{p}$ must lie and then determines $\hat{p}$ by bisection along the linear interpolation between p_l and p_{l+1}, such that the respective headpoints satisfy

$$(1-\varepsilon)\Delta_k < |P(\hat{p}(0)) - p_k(0)| < (1+\varepsilon)\Delta_k, \tag{5}$$

where ε is a pre-specified tolerance. In fact, one can take ε relatively large without loss of accuracy, which makes the method more efficient by reducing the number of bisection steps dramatically [23]. The linear interpolation between p_l and p_{l+1} is defined pointwise for all $t \in [-\tau, 0]$.

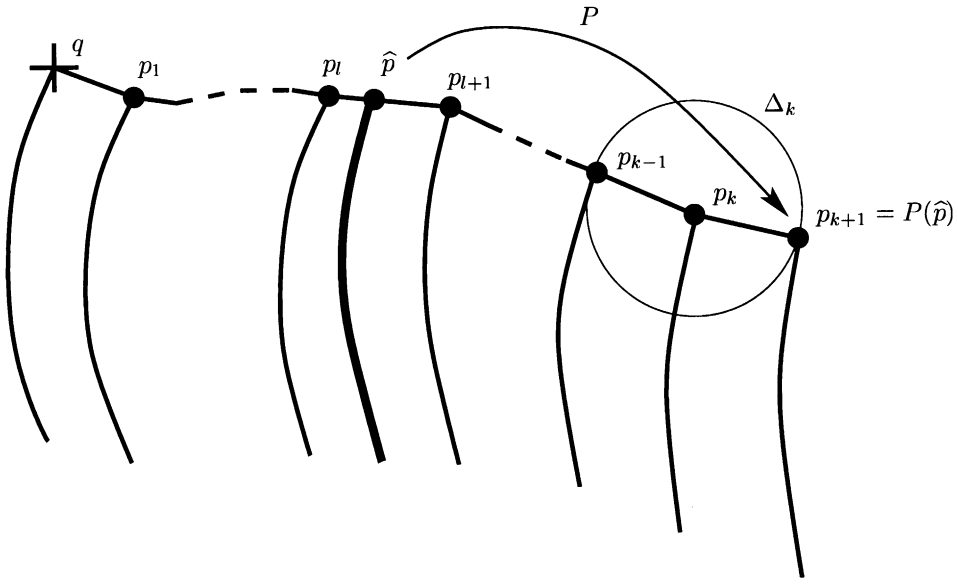

Fig. 6. Sketch of the algorithm. The new point p_{k+1} lies at distance Δ_k from p_k, and it is found as the image of an interpolated point $\hat{p}$ on the part of $W^{\mathrm{u}}(q)$ that was already computed. To indicate that we are dealing with a DDE we sketch this situation in physical space; the headpoint of each point lies in the section Σ.

The distance Δ_k is adapted during the computation depending on the curvature of the trace of the manifold $W^{\mathrm{u}}(q) \cap \Sigma$ in the section Σ. This is done because we want to represent the trace faithfully with as few points as possible; see Section 3.3 for a discussion of what this means in terms of the accuracy of our method. We use a criterion first used in [23] to accept the new point; for details see also [18]. The quantity

$$\alpha_k = \frac{|\bar{p}(0) - p_{k-1}(0)|}{|p_k(0) - p_{k-1}(0)|} \tag{6}$$

is an approximation of the angle α between the line segments from $p_{k-1}(0)$ to $p_k(0)$ and from $p_k(0)$ to $p_{k+1}(0)$, where

$$\bar{p}(0) = p_k(0) + |p_k(0) - p_{k-1}(0)| \frac{(p_k(0) - p_{k+1}(0))}{|p_k(0) - p_{k+1}(0)|}. \tag{7}$$

Note that the angle is only computed in the section Σ.

The key is to check the conditions

$$\alpha_{\min} < \alpha_k < \alpha_{\max}, \tag{8}$$

$$(\Delta\alpha)_{\min} < \Delta_k \alpha_k < (\Delta\alpha)_{\max}, \tag{9}$$

where the bounds are four pre-specified accuracy parameters. Condition (8) states that α_k should be small, while condition (9) controls the local interpolation error.

If both $\alpha_k < \alpha_{\max}$ and $\Delta_k \alpha_k < (\Delta\alpha)_{\max}$ then Δ_k is acceptable and the point $P(\hat{p})$ is accepted as the new point p_{k+1}. We keep the estimate for Δ_k unchanged, that is, $\Delta_{k+1} = \Delta_k$, except if both $\alpha_k < \alpha_{\min}$ and $\Delta_k \alpha_k < (\Delta\alpha)_{\min}$. Then we set $\Delta_{k+1} = 2\Delta_k$. If $\alpha_k \geqslant \alpha_{\max}$ or $\Delta_k \alpha_k \geqslant (\Delta\alpha)_{\max}$ then Δ_k is too large and p_{k+1} is not accepted. We set $\Delta_k = \frac{1}{2}\Delta_k$ and find a new candidate. At sharp bends of the manifold it may not be possible to ensure that $\alpha_k \geqslant \alpha_{\max}$ without making Δ_k impractically small. In this case, we accept the candidate p_{k+1} after all if $\Delta_k < \Delta_{\min}$ for a pre-specified number $\Delta_{\min}$. By choosing these accuracy parameters suitably, one can ensure that bends do not get cut off; see the discussion in [23].

The computation stops after a prescribed arclength distance of the trace $W^{\mathrm{u}}(q) \cap \Sigma$ has been reached. However, it may be that $W^{\mathrm{u}}(q) \cap \Sigma$ does not have such a large arclength, which occurs typically when the manifold ends up at an attracting fixed point. Convergence of new points on the manifold is detected when Δ_k dips under a pre-specified value and the computation also stops.

3.3. On the accuracy

By a computation we mean the computation of a piece of one branch of $W^{\mathrm{u}}(q)$ up to some prescribed arclength. When computing a global invariant manifold it is generally impossible to derive a priori bounds on the accuracy parameters one needs to choose in order to achieve a given accuracy. Furthermore, the accuracy of a calculation generally becomes worse as longer pieces of $W^{\mathrm{u}}(q)$ are computed; compare [21–23]. Therefore, the only practical way of checking the accuracy of a computation in practice is to repeat it with increased accuracy and to compare the results. If the difference between the two approximations of $W^{\mathrm{u}}(q)$ is smaller than some user-defined bound, then the computation can be accepted as accurate enough. This is certainly the strategy a user should adopt when using the algorithm presented here.

In the examples below we used a different method to illustrate the accuracy of our computations, namely to overlay points obtained by fundamental domain iteration, also starting from $q \pm \delta v$. While these overlaid points are not well distributed along $W^{\mathrm{u}}(q)$, their computation does involve only integration, and not interpolation. It is therefore a good test to check that these points all lie on the approximation of $W^{\mathrm{u}}(q)$ computed with our method; see already Section 4.3.

We now discuss briefly what contributes to the error of a computation, where we follow [23]. The first contribution to the overall error depends on the initial distance δ along $E^{\mathrm{u}}(q)$ and on the distribution of mesh points along $W^{\mathrm{u}}(q)$. As is the case for the algorithm for finite-dimensional maps, the initial error between $q \pm \delta v$ and $W^{\mathrm{u}}_{\mathrm{loc}}(q)$ goes to zero with δ. Note that v is only known approximately, but the difference between v and $E^{\mathrm{u}}(q)$ can be made arbitrarily small. Further, $W^{\mathrm{u}}(q)$ is a collection of P-images of $W^{\mathrm{u}}_{\mathrm{loc}}(q)$ and, due to the hyperbolicity of q, $W^{\mathrm{u}}(q)$ is attracting in some neighborhood U of q, so that the initial error will be damped in this neighborhood. However, outside U the initial error grows with the number of iterates that are needed to cover the computed part of $W^{\mathrm{u}}(q)$.

Outside U the total integration time is bounded from above implicitly by the maximal integration time used to compute (the finitely many iterations of) the Poincaré map. Therefore, the numerical integration is supposed to be accurate enough so that the integration error makes a negligible contribution to the overall error of the computation.

Because the manifold is grown by taking images of interpolated points, the interpolation error ε_{I} between the mesh points is important. The key thing is to keep the distance between two consecutive mesh points p_l and p_{l+1} small, depending on the curvature of $W^{\mathrm{u}}(q)$. It would be possible to check the curvature pointwise between three consecutive points for all points along the history, that is, for all $t \in [-\tau, 0]$. However, this would be computationally very expensive. Therefore, we chose to let Δ_k, the distance to the next point, depend only on the curvature of the trace $W^{\mathrm{u}}(q) \cap \Sigma$. As in the finite-dimensional case, the distance, and hence the local interpolation error, between the headpoints $p_l(0)$ and $p_{l+1}(0)$ is controlled by keeping the product $\Delta_k \alpha_k$ small; see [18,23].

The main reason for considering only the curvature of the trace is the following. It is ultimately the trace that we want to work with in applications, so that it makes sense to represent it well with as few points as possible. But further, this strategy also ensures that the local interpolation error between a pair of points p_l and p_{l+1} is bounded not just for $t = 0$ but for all $t \in [-\tau, 0]$, because the error $|p_{l+1}(t) - p_l(t)|$ depends continuously in t on $|p_{l+1}(0) - p_l(0)|$. Clearly, the error $|p_{l+1}(t) - p_l(t)|$ can be very large, but it does go to zero with $|p_{l+1}(0) - p_l(0)|$. Therefore, over a finite computation, the overall interpolation error is bounded.

We found that our strategy works well for the examples we considered: indeed the distance between p_l and p_{l+1} is nicely bounded for all l and $t \in [-\tau, 0]$, as can be seen in Fig. 11 below. We repeat that it is impossible to find a priori error bounds for this error, so that a computation should not be trusted blindly. Instead, as mentioned above, one should check the accuracy by increasing the accuracy bounds.

4. Example: the PCF laser

To illustrate the performance of our algorithm, we consider a semiconductor laser receiving *phase-conjugate feedback* (PCF) from a phase-conjugating mirror (PCM) [1]; see Fig. 7. This form of feedback

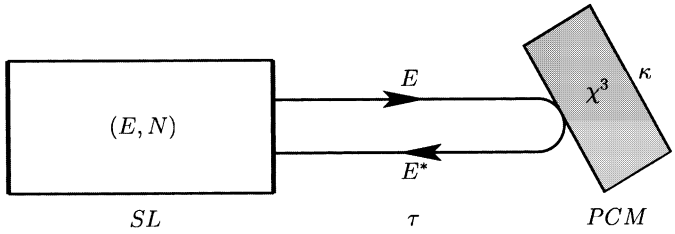

Fig. 7. Sketch of a semiconductor laser with phase-conjugate feedback.

is physically interesting as it produces a return wave which coincides exactly with the incident wave, so that the system is self-aligning. Furthermore, due to the phase-conjugating nature of the mirror, distortions are undone on the return trip in the external cavity. This system, the PCF laser in short, has been used as a stable (high-power) source in applications, for example, for frequency control and mode-switching [3,33].

The PCF laser is a technologically relevant example of a DDE. Its physical space is three-dimensional, that is, $n = 3$ in (1), and this has the advantage of allowing for good illustrating figures in $\mathbb{R}^3$. Apart from its stable operation, the PCF laser was shown to exhibit complicated nonlinear dynamics, including stable periodic operation, quasiperiodic motion and chaos. This was found in detailed simulations of bifurcation diagrams, phase plots and optical spectra [13,19]. As the feedback strength is increased, the overall picture is that of regions of periodic output that are interspersed with 'bubbles' of chaos. In order to understand in more detail the nature of different transitions to chaos one needs to use new numerical techniques, namely the combination of DDE-BIFTOOL with the manifold computations introduced here. The results of this ongoing effort will be published elsewhere [14,15]. Here we use the PCF laser to illustrate the computation of one-dimensional unstable manifolds.

4.1. Rate equations

A single-mode semiconductor laser subject to weak (instantaneous) PCF is modeled by the rate equations

$$\frac{\mathrm{d}E(t)}{\mathrm{d}t} = \frac{1}{2}\left[-\mathrm{i}\alpha G_N(N(t) - N_{\mathrm{sol}}) + \left(G(t) - \frac{1}{\tau_p}\right)\right]E(t) + \kappa E^*(t-\tau)\exp[\mathrm{i}\phi_{\mathrm{PCM}}], \tag{10}$$

$$\frac{\mathrm{d}N(t)}{\mathrm{d}t} = \frac{I}{q} - \frac{N(t)}{\tau_e} - G(t)|E(t)|^2, \tag{11}$$

for the evolution of the slowly varying complex electric field $E(t) \in \mathbb{C}$ and the population inversion $N(t) \in \mathbb{R}$ [19]; E^* is standard physical notation for the complex conjugate of E. Nonlinear gain is included as $G(t) = G_N(N(t) - N_0)(1 - \epsilon P(t))$, where $\epsilon = 3.57 \times 10^{-8}$ is the nonlinear gain coefficient and $P(t) = |E(t)|^2$ is the intensity. The different parameters are set to realistic values of a Ga–Al–As semiconductor laser [13,19], namely the line-width enhancement factor $\alpha = 3$, the optical gain $G_N = 1190\,\mathrm{s}^{-1}$, the photon lifetime $\tau_p = 1.4\,\mathrm{ps}$, the injection current $I = 65.1\,\mathrm{mA}$, the magnitude of the electron charge $q = 1.6 \times 10^{-19}\,\mathrm{C}$, the electron lifetime $\tau_e = 2\,\mathrm{ns}$, and the transparency electron number $N_0 = 1.64 \times 10^8$. The phase shift ϕ_{PCM} was set to zero and $N_{\mathrm{sol}} = N_0 + 1/(G_N\tau_p)$. The delay (the external cavity round-trip time) τ was fixed at $\tau = 2/3\,\mathrm{ns}$ and the feedback rate κ is the main bifurcation parameter.

In what follows we consider the dependence of (10) on the dimensionless bifurcation parameter $\kappa\tau$. To obtain a range of order 1 of the E and N values covered by the periodic orbits we consider, we rescaled $E(t)$ by a factor of 1.0×10^{-2} and $N(t)$ by a factor of 1.0×10^{-6}. This does not change any of the dynamics, but is important during our computations of unstable manifolds.

System (10) is symmetric under the transformation $E \to -E$, which is the rotation of the E-plane by π. Any attractor or other invariant set is either symmetric, or has a symmetric counterpart [19,25]. This has consequences for the types of bifurcations that can occur. In particular, when a Floquet multiplier of a symmetric periodic orbit goes through $+1$ then this may indicate a symmetry breaking bifurcation [15] rather than a saddle-node bifurcation of limit cycles.

The number of discretization intervals was set to $M = 2500$ for all computations in this paper (giving an integration step of $\tau/2500$). In other words, every point $q \in \mathscr{C}$ was represented by a circular list with 2504 list elements, each consisting of three double-precision numbers to store E and N.

4.2. The bifurcation diagram

To illustrate our method we focus on a transition to chaos via the break-up of a torus in the interval $\kappa\tau \in [2.3, 2.6]$. In the notation of [13,19], this occurs at the beginning of the second 'bubble' of complicated dynamics. More details on the dynamics associated with the bifurcations of this torus can be found in [15].

The bifurcation diagram in Fig. 8(a) was obtained by simulation: for a new value of $\kappa\tau$ we integrated (10) starting from the attractor for the previous $\kappa\tau$, let transients die away, and then plotted $\hat{N} = (N/N_{\mathrm{sol}} - 1) \times 10^3$ whenever the intensity $P(t) = |E(t)|^2$ crossed its average value in the positive direction [19]. Fig. 8(a) tells one what happens to the (main) attractor. It seems that a periodic orbit becomes unstable when a torus is born, the dynamics on this torus appears to be quasiperiodic at first, but then locks to a periodic orbit as five distinct branches appear. This new periodic orbit seems to undergo a torus bifurcation of its own. The new torus then suddenly disappears and a region of chaos is entered. We remark that there is no hysteresis when changing the direction of the sweep in $\kappa\tau$.

As a first step to understand what is going on we started a DDE-BIFTOOL computation from the stable locked periodic orbit for $\kappa\tau = 2.445$ that we found by numerical integration. The result is shown in Fig. 8(b), where the period of the respective periodic orbit is plotted against $\kappa\tau$. At $\kappa\tau \approx 2.441$ a stable and a saddle periodic orbit are born on the torus in a saddle-node bifurcation of limit cycles, which corresponds to the beginning of locked dynamics. The stable periodic orbit disappears in a torus bifurcation T that is detected at $\kappa\tau \approx 2.556$. The bifurcating torus is stable and it is like a hose winding around the original torus; see [15] for more details. Both the stable and the saddle periodic orbits undergo symmetry breaking bifurcations at the points denoted *SB*. They are in fact connected by a branch of non-symmetric periodic orbits; see [15] for details. On the lower branch between the points *SL* and *SB* the unstable periodic orbit has exactly one unstable Floquet multiplier.

4.3. One-dimensional unstable manifolds

Our method is implemented in C++ and its performance is demonstrated with the one-dimensional unstable manifolds of periodic points associated with the periodic orbit in Fig. 4 of the PCF laser (10) for $\kappa\tau = 2.500$.

The periodic point q in Figs. 3 and 4 has the one-dimensional unstable linear eigenspace $E^{\mathrm{u}}(q)$ shown in Fig. 5. It was computed as described in Section 3.1 and stored in the normalised vector v. The computation

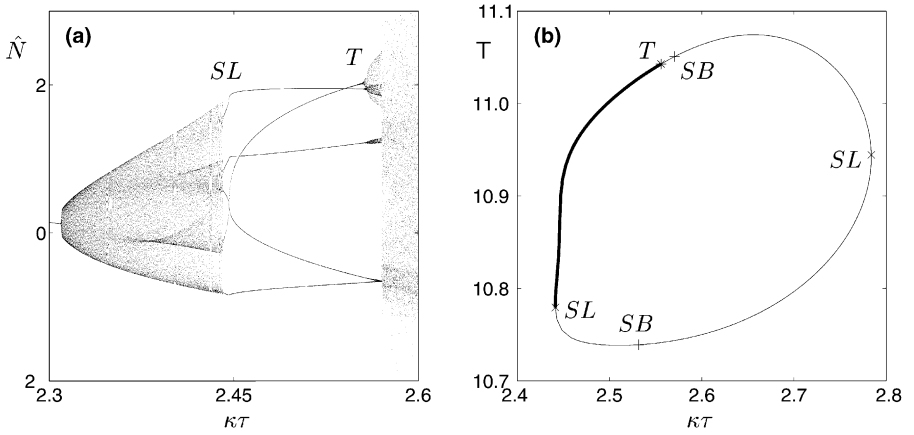

Fig. 8. The bifurcation diagram for $\kappa\tau \in [2.3, 2.6]$ found by simulation (a), and the continuation with DDE-BIFTOOL of periodic orbits for $\kappa\tau \in [2.4, 2.8]$ (b).

of $W^{\mathrm{u}}(q)$ was started at a distance $\delta = 1.0 \times 10^{-4}$, while the accuracy parameters (detailed in Section 2.4) were $\alpha_{\min} = 0.2$, $\alpha_{\max} = 0.3$, $(\Delta\alpha)_{\min} = 1.0 \times 10^{-3}$, $(\Delta\alpha)_{\max} = 1.0 \times 10^{-4}$, $\Delta_{\min} = 1.0 \times 10^{-2}$ and $\varepsilon = 0.2$. Convergence of the manifold to a stable periodic orbit was detected when Δ_k fell below 5.0×10^{-4}.

Fig. 9(a) shows the trace in the section Σ defined by $N = 762.0$. The points that were computed are shown in Fig. 9(b), illustrating the distribution of points along $W^{\mathrm{u}}(q) \cup \Sigma$ according to its curvature. Fig. 9(c) shows points obtained by iterating 100 initial points in a fundamental domain. While their distribution is such that one does not obtain a good image of the manifold, they lie on the trace of the true manifold to within the accuracy of integration. Indeed, an overlay of panels (a) and (c) in Fig. 9(d) demonstrates the accuracy of the computed trace; the distance of the iterated points to the computed branch is less than 1.5×10^{-3}. Note that the trace has self-intersections and sharp bends, which are both due to the projection, and eventually spirals into an attracting periodic point.

Fig. 10(a) shows the overall picture with all branches of all five periodic points corresponding to the periodic orbit, rendered from the computed points in Fig. 10(b). Points obtained by fundamental domain iteration in Fig. 10(c) again lie on the computed one-dimensional trace, as is illustrated in Fig. 10(d). The five saddle points are mapped to each other by the fourth return to Σ. The unstable manifolds converge to five attracting equilibria, which correspond to the five branches in Fig. 8(a).

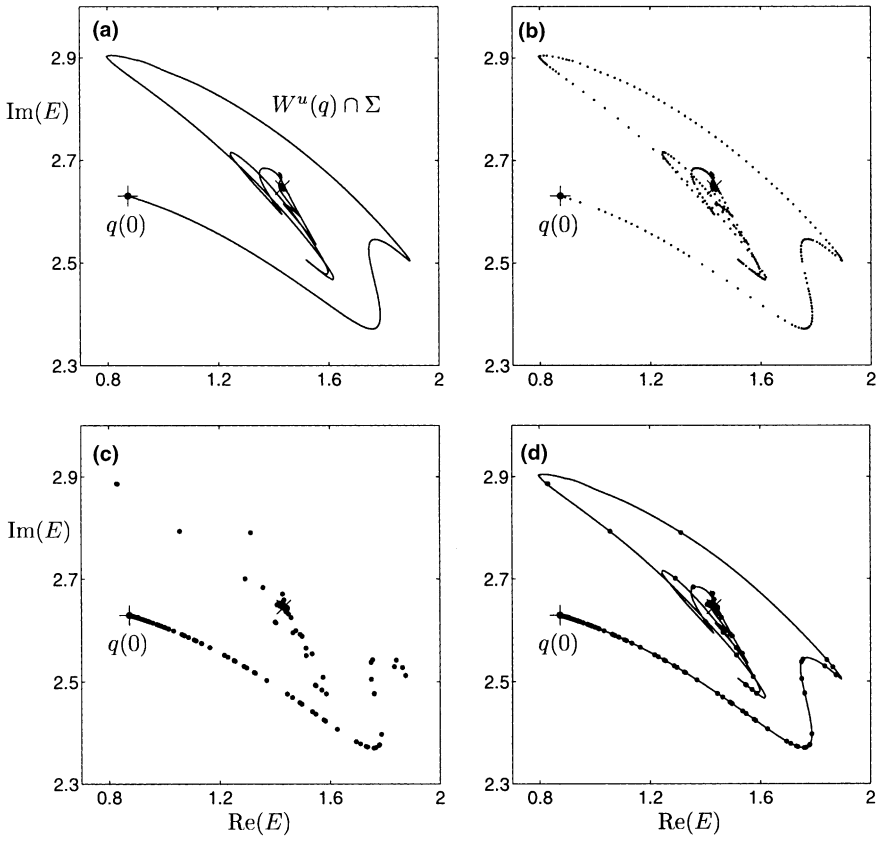

Fig. 9. The trace of one branch of the unstable manifold of the saddle-point (+), which spirals into an attractor (×). Shown is the branch computed by our algorithm (a), the distribution of points along this branch (b), and the branch computed by fundamental domain iteration (c). Part (d) shows that all points of (c) lie exactly on the computed branch from (a). This branch is for $\kappa\tau = 2.500$ and it is one of the branches in Fig. 10.

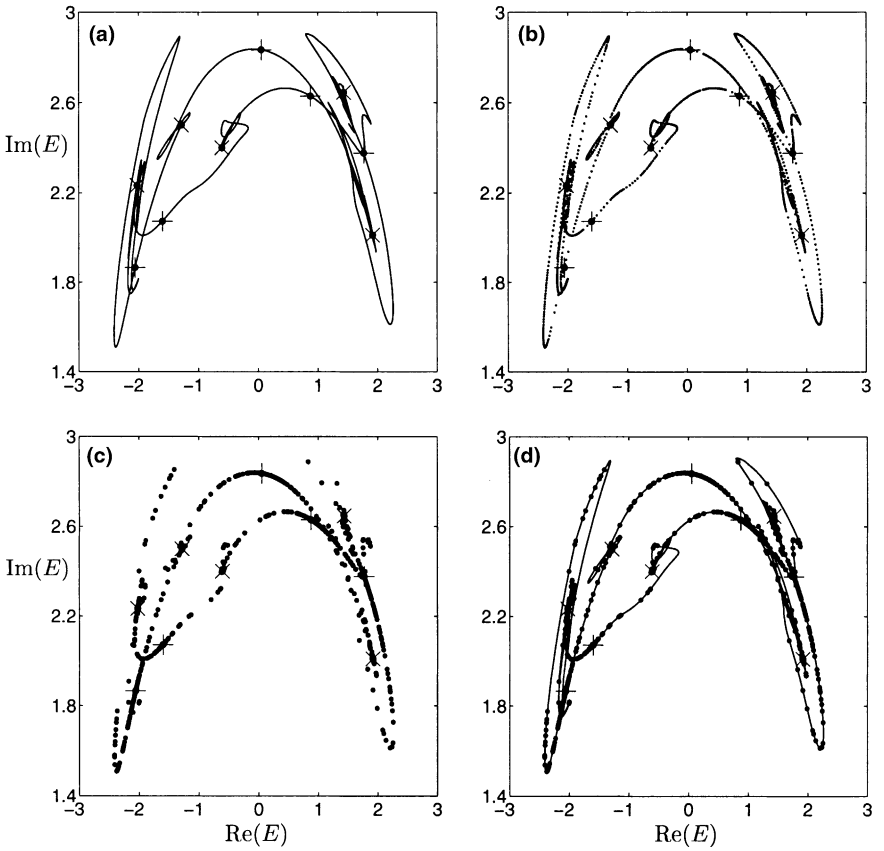

Fig. 10. The traces of all branches in Σ emanating from both sides of the five saddle-points (+) converging to five attractors ($\times$) for $\kappa\tau = 2.500$. Panels (a)–(d) illustrate the performance of our algorithm as in Fig. 9.

Finally, we show in Fig. 11 the manifolds corresponding to the traces in Figs. 9 and 10 in projection onto (E, N)-space (left column) and onto the E-plane (right column). This reveals their intricate structure and highlights their high-dimensional nature. One can imagine the one-dimensional trace in Σ as a 'curtain rail' along which the 'curtain' $W^{\mathrm{u}}(q)$, made up of the headpoints in Figs. 9(b) and 10(b) together with their histories, is drawn during the growth process. This is shown in an animation accompanying this paper, which can be accessed at http://www.enm.bris.ac.uk/staff/berndk/ddeman.html.

The manifolds in Fig. 10(a) form a continuous curve, which is in fact what is left of the torus after locking. A detailed study of the bifurcations of this torus can be found in [15]. Here we merely demonstrate the usefulness of our algorithm in Fig. 12 with the traces in the section Σ of all branches of the one-dimensional unstable manifolds of five saddle points for four increasing values of $\kappa\tau$. This reveals the classic picture of locking on a smooth torus in Fig. 12(a). However, as $\kappa\tau$ is increased the unstable manifolds start to spiral into the five attracting equilibria, a sign that the torus has lost its smoothness; see Fig. 12(b), where $\kappa\tau = 2.450$. When $\kappa\tau$ is increased even further the manifolds develop into an increasingly complicated shape as in Fig. 12(c) and (d) for $\kappa\tau = 2.480$ and $\kappa\tau = 2.500$, respectively (note that Figs. 9 and 10 correspond to Fig. 12(d)). This is a precursor of a crisis bifurcation, which is responsible for the sudden transition to chaos that is apparent in Fig. 8.

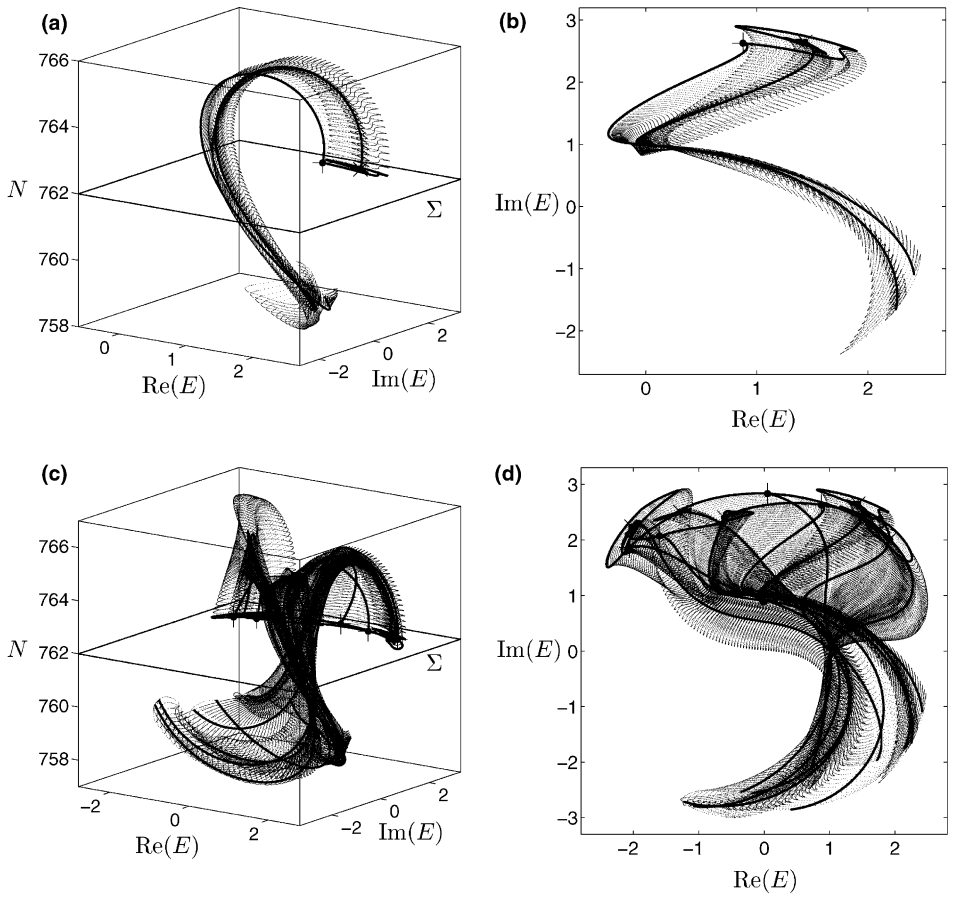

Fig. 11. One branch of the unstable manifold (shown in Fig. 9 in the section Σ) in (E,N)-space (a) and in the E-plane (b), and all branches emanating from both sides of the five saddle-points (shown in Fig. 10 in the section Σ) in (E,N)-space (c) and in the E-plane (d).

Fig. 13 shows the development of a single branch of the unstable manifold of a fixed point when $\kappa\tau$ is changed through the symmetry breaking bifurcation *SB* on the lower branch in Fig. 8. Fig. 13(d) corresponds to a situation where there are two unstable eigenvalues, the one that is involved in the symmetry breaking being very small. As was explained in Section 3.1, our method computes the strong unstable manifold in this case. As is evident from Fig. 13, the strong unstable manifold is the continuation of the one-dimensional unstable manifold before the bifurcation. This is the case as long as the same unstable eigenvalue remains the strongest one.

Finally, Fig. 14(a) shows the trace of one branch of an unstable manifold that encounters interior tangencies where the kth return map is discontinous. Near the fixed point q, where the computation starts, P is defined as the 20th return to Σ. However, the boldfaced part of the trace corresponds to points where P is defined as the 18th return to Σ. In Fig. 14(b) we plotted the integration time for each computed point, and this clearly shows that, although the number of returns to Σ varies along the branch, the integration time is a continuous function. In other words, we are indeed following the right branch of P. As mentioned in Section 2.3, this technique of adapting the number of returns to the section during a computation allows one to compute longer pieces of $W^{\mathrm{u}}(q)$.

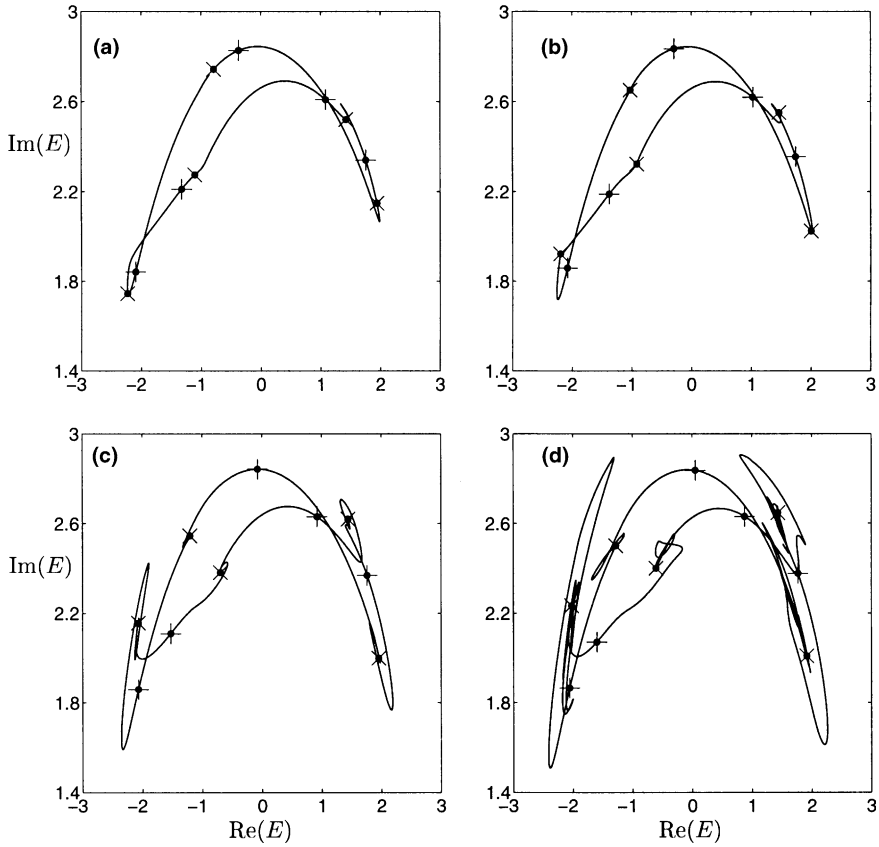

Fig. 12. As $\kappa\tau$ is increased, the smooth torus at $\kappa\tau = 2.445$ (a) loses its smoothness at $\kappa\tau = 2.450$ (b). As $\kappa\tau$ is increased further through $\kappa\tau = 2.480$ (c) and $\kappa\tau = 2.500$ (d), the torus becomes increasingly folded and stretched.

5. Conclusions

We presented an algorithm for computing one-dimensional unstable manifolds of saddle fixed points of a Poincaré map of a DDE, which generalizes the method for finite-dimensional maps in [23] to Poincaré maps of DDEs. Behind this is the idea to work with points in the infinite-dimensional phase space of the DDE just like with points in a finite-dimensional space. While this sounds simple, it requires the extension of all operations, such as computing the Poincaré map or interpolation, to the infinite-dimensional setting, which can be achieved by performing the respective operation *pointwise* along the entire history of a point. Note that computations for DDEs are much more data intensive than those for ODEs or maps, because one needs to deal with (the discretizations of) all histories. Our method uses DDE-BIFTOOL to generate the starting data, and it is planned to combine continuation and manifold computations.

Any method for growing unstable manifolds in ODEs or maps could be generalized in the same way to DDEs or their Poincaré maps. We have taken here the first step by computing one-dimensional unstable manifolds of saddle points. It is an interesting challenge for future work to compute two-dimensional unstable manifolds of equilibria by generalizing the method in [24], and two-dimensional unstable manifolds of saddle fixed points (corresponding to periodic orbits of the DDE) by generalizing that in [21].

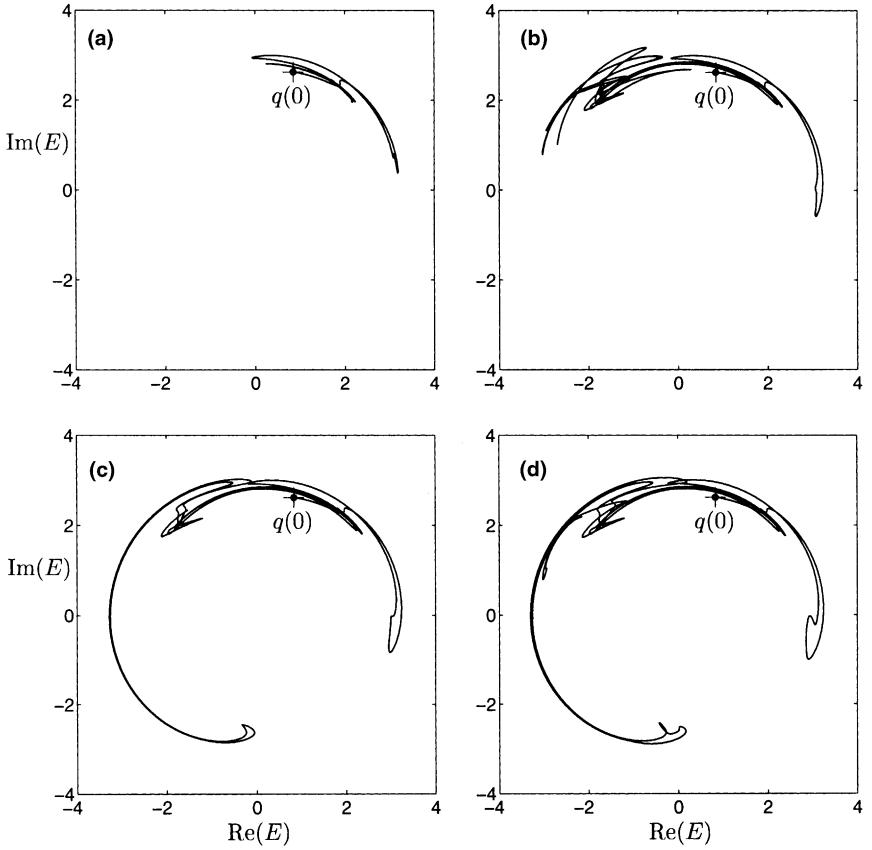

Fig. 13. Trace of one branch of the unstable manifold of the saddle-point q for $\kappa\tau = 2.5197$ (a), $\kappa\tau = 2.5271$ (b), $\kappa\tau = 2.5310$ (c), and the trace of the strong unstable manifold for $\kappa\tau = 2.5348$ (d).

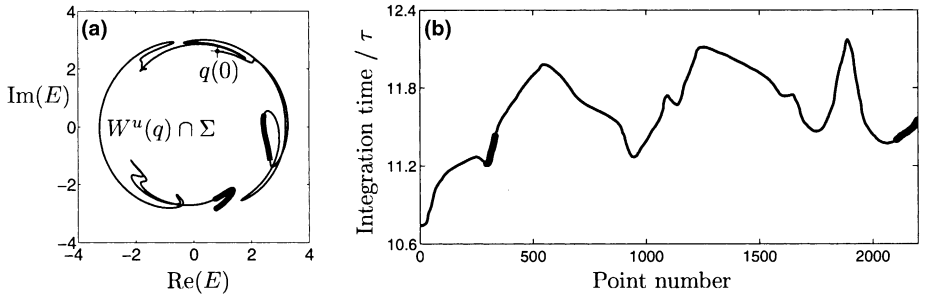

Fig. 14. Trace of a single branch of the unstable manifold for $\kappa\tau = 2.550$ (a) covering a large area. The Poincaré map is normally the 20th return to Σ, but along the boldfaced sections it is the 18th return to Σ. Nevertheless, the integration time for each point along the branch is a continuous function (b).

The performance of our method was demonstrated with the rate equation model (10) of a semiconductor laser subject to phase-conjugate feedback. The physical space of this system is three-dimensional, so that the condition defining the Poincaré section Σ corresponds to a two-dimensional plane in physical space.

This is very helpful because the traces of the respective manifolds look just like one-dimensional unstable manifolds of a planar map. However, there will generally be self-intersections and isolated points of non-smoothness due to projection, which are a reminder of the inherently infinite-dimensional nature of the problem. While it is useful to work with a three-dimensional projection, we remark that it is not necessary that the *physical space* is three-dimensional. Alternatively, one can consider any three-dimensional space onto which one projects the infinite-dimensional phase space of the DDE, so that Σ again defines a two-dimensional subspace in this space.

Combined with the continuation of saddle periodic orbits, the computation of one-dimensional manifolds presented here allows one to study *global bifurcations* in DDEs for the first time in much the same spirit as one does in ODEs. This was demonstrated here with the example of the break-up of a torus and a subsequent crisis bifurcation to chaos; further details can be found in [15]. In ongoing research we investigate other global bifurcations and transitions to chaos in the PCF laser. The method presented here contributes to the theory of global bifurcations in DDEs, and will be equally useful for the study of other systems with delay.

Acknowledgements

We thank Koen Engelborghs for his help with DDE-BIFTOOL and Hinke Osinga for helpful comments. B.K. is supported by an EPSRC Advanced Research Fellowship.

References

[1] G.P. Agrawal, G.R. Gray, Effect of phase-conjugate feedback on the noise characteristics of semiconductor lasers, Phys. Rev. A 46 (1992) 5890.
[2] A. Back, J. Guckenheimer, M. Myers, F. Wicklin, P. Worfolk, DsTool: computer assisted exploration of dynamical systems, Notices AMS 39 (4) (1992) 303.
[3] N. Cyr, M. Breton, M. Tetu, S. Theriault, Laser-diode frequency control by resonant phase-conjugate reflection from an atomic vapor, Opt. Lett. 16 (1991) 1298.
[4] O. Diekmann, S.A. Gils, S.M. Verduyn Lunel, H.O. Walther, Delay Equations: Functional-, Complex-, and Nonlinear Analysis, Applied Mathematical Sciences, vol. 110, Springer-Verlag, New York, 1995.
[5] E. Doedel, T. Fairgrieve, B. Sandstede, A. Champneys, Y.u. Kuznetsov, X. Wang, AUTO 97: Continuation and bifurcation software for ordinary differential equations', http://indy.cs.concordia.ca/auto/main.html.
[6] K.-J. Engel, R. Nagel, One-parameter Semigroups for Linear Evolution Equations, Graduate Texts in Mathematics, vol. 194, Springer-Verlag, New York, 2000.
[7] K. Engelborghs, T. Luzyanina, G. Samaey, DDE-BIFTOOL v2.0: a Matlab package for bifurcation analysis of delay differential equations, 2001 http://www.cs.kuleuven.ac.be/~koen/delay/ddebiftool.shtml.
[8] K. Engelborghs, T. Luzyanina, K. in't Hout, D. Roose, Collocation methods for the computation of periodic solutions of delay differential equations, SIAM J. Sci. Comput. 22 (2000) 1593.
[9] K. Engelborghs, T. Luzyanina, D. Roose, Numerical bifurcation analysis of delay differential equations, J. Comput. Appl. Math. 125 (2000) 265.
[10] I. Fischer, T. Heil, W. Elsäßer, Emission dynamics of semiconductor lasers subject to delayed optical feedback, in: B. Krauskopf, D. Lenstra (Eds.), Fundamental Issues of Nonlinear Laser Dynamics, AIP Conf. Proc., vol. 548, 2000, p. 218.
[11] A. Gavrielides, Nonlinear dynamics of semiconductor lasers: theory and experiments, in: B. Krauskopf, D. Lenstra (Eds.), Fundamental Issues of Nonlinear Laser Dynamics, AIP Conf. Proc., vol. 548, 2000, pp. 191–217.
[12] H. Glusing-Luerssen, A behavioural approach to delay-differential systems, SIAM J. Control Optim. 35 (1997) 480.
[13] G.R. Gray, D. Huang, G.P. Agrawal, Chaotic dynamics of semiconductor lasers with phase-conjugate feedback, Phys. Rev. A 49 (1994) 2096.
[14] K. Green, B. Krauskopf, Global bifurcations and bistability at the locking boundaries of a semiconductor laser with phase-conjugate feedback, Phys. Rev. E 66 (2002) 016220.
[15] K. Green, B. Krauskopf, K. Engelborghs, Bistability and torus break-up in a semiconductor laser with phase-conjugate feedback, Physica D 173 (2002) 114–129.

[16] J.K. Hale, S.M. Verduyn Lunel, Introduction to Functional Differential Equations, Springer-Verlag, New York, 1993.
[17] T. Heil, I. Fischer, W. Elsäßer, Chaos synchronization and spontaneous symmetry-breaking in symmetrically delay-coupled semiconductor lasers, Phys. Rev. Lett. 86 (5) (2001) 795–798.
[18] D. Hobson, An efficient method for computing invariant manifolds of planar maps, J. Comput. Phys. 104 (1993) 14–22.
[19] B. Krauskopf, G.R. Gray, D. Lenstra, Semiconductor laser with phase-conjugate feedback: dynamics and bifurcations, Phys. Rev. E 58 (6) (1998) 7190–7196.
[20] B. Krauskopf, D. Lenstra (Eds.), Fundamental Issues of Nonlinear Laser Dynamics, AIP Conf. Proc. 548 (2000).
[21] B. Krauskopf, H.M. Osinga, Globalizing two-dimensional unstable manifolds of maps, Int. J. Bifurc. Chaos 8 (3) (1998) 483–503.
[22] B. Krauskopf, H.M. Osinga, Investigating torus bifurcations in the forced Van der Pol oscillator, in: E.J. Doedel, L.S. Tuckerman (Eds.), Numerical Methods for Bifurcation Problems and Large-Scale Dynamical Systems, IMA Volumes in Mathematics and its Applications, vol. 119, Springer-Verlag, New York, 2000, pp. 199–208.
[23] B. Krauskopf, H.M. Osinga, Growing 1D and quasi-2D unstable manifolds of maps, J. Comput. Phys. 146 (1998) 404.
[24] B. Krauskopf, H.M. Osinga, Two-dimensional global manifolds of vector fields, Chaos 9 (3) (1999) 768–774.
[25] B. Krauskopf, G.H.M. van Tartwijk, G.R. Gray, Symmetry properties of lasers subject to optical feedback, Opt. Commun. 177 (2000) 347–353.
[26] D. Lenstra, M. Yousefi, Theory of delayed optical feedback in lasers, in: B. Krauskopf, D. Lenstra (Eds.), Fundamental Issues of Nonlinear Laser Dynamics, AIP Conf. Proc. 548 (2000) 87–111.
[27] C.M. Marcus, R.M. Westervelt, Stability of analog networks with delay, Phys. Rev. A 39 (1989) 347.
[28] J.D. Murray, Mathematical Biology, Biomathematics Texts, vol. 19, Springer-Verlag, Berlin, 1980.
[29] T.S. Parker, L.O. Chua, Practical Numerical Algorithms for Chaotic Systems, Springer-Verlag, New York/Berlin, 1989.
[30] D. Pieroux, T. Erneux, B. Haegeman, K. Engelborghs, D. Roose, Bridges of periodic solutions and tori in semiconductor lasers subject to delay, Phys. Rev. Lett. 87 (2001) 193901.
[31] D. Pieroux, T. Erneux, T. Luzyanina, K. Engelborghs, Interacting pairs of periodic solutions lead to tori in lasers subject to delayed feedback, Phys. Rev. E 63 (2001) 036211.
[32] G. Samaey, K. Engelborghs, D. Roose, Numerical computation of connecting orbits in delay differential equations, Numer. Algorithms 30 (2002) 335–352.
[33] T. Shimura, M. Tamura, K. Kuroda, Injection locking and mode switching of a diode laser with a double phase-conjugate mirror, Opt. Lett. 18 (1993) 1645.
[34] S.M. Verduyn Lunel, B. Krauskopf, The mathematics of delay equations with an application to the Lang–Kobayashi equations, in: B. Krauskopf, D. Lenstra (Eds.), Fundamental Issues of Nonlinear Laser Dynamics, AIP Conf. Proc. 548 (2000) 66–86.
[35] X.S. Yao, L. Maleki, Dual microwave and optical oscillator, Opt. Lett. 22 (1997) 1867.
[36] Z. You, E.J. Kostelich, J.A. Yorke, Calculating stable and unstable manifolds, Int. J. Bifurc. Chaos 1 (1991) 605.